Mechanical behavior of a chromium coating on a zirconium alloy substrate at room temperature

Duc Vinh Nguyen, Matthieu Le Saux, Lionel Gélébart, Jean-Christophe Brachet, Jean-Philippe Bonthonneau, Arnaud Courcelle, Raphaelle Guillou, Elodie Rouesne, Stephane Urvoy

Version of Record: https://www.sciencedirect.com/science/article/pii/S0022311521005559
Manuscript_3ff9b0403238bc8b7b038ec626ec4e5a

Mechanical behavior of a chromium coating on a zirconium alloy substrate at room temperature

Duc Vinh Nguyen[a], Matthieu Le Saux[a,b], Lionel Gélébart[a,*], Jean-Christophe Brachet[a], Jean-Philippe Bonthonneau[a], Arnaud Courcelle[c], Raphaelle Guillou[a], Elodie Rouesne[a] and Stephane Urvoy[a]

[a]*Université Paris-Saclay, CEA, DES - Service de Recherches Métallurgiques Appliquées, F-91191, Gif-sur-Yvette, France*
[b]*Now at ENSTA Bretagne, UMR CNRS 6027, IRDL, F-29200, Brest, France*
[c]*Université Paris-Saclay, CEA, DES - Service dâĂŹEtude des Matériaux Irradiés, F-91191, Gif-sur-Yvette, France*

ARTICLE INFO

Keywords:
Enhanced accident tolerant fuel claddings
Chromium coating
Cracking
Plasticity
Digital Image Correlation
Biaxial tests

ABSTRACT

The mechanical behavior of a 15 Âţm-thick chromium coating deposited on a zirconium alloy substrate using a particular physical vapor deposition process is studied at room temperature using several experimental techniques at different scales: biaxial tests (internal pressure + axial tension) with several stress biaxiality ratios on outer-coated tubes; *in situ* tensile tests in a scanning electron microscope (SEM) on coated sheet samples. The cracking and plasticity of the coating are studied using acoustic emission, digital image correlation and SEM observations. The results show that the first channeling cracks in the coating initiate at 0.3-0.4% macroscopic strain, when the substrate starts to yield. Under further loading, the crack density increases first rapidly then more slowly, before reaching saturation. Plastic strain of the non-cracked coating regions is observed, in addition to the increase of crack opening. No interface decohesion of the coating is observed. The cracks, both transgranular and intergranular, do not penetrate significantly into the substrate.

1. Introduction

The 2011 Fukushima Daiichi nuclear disaster raised worldwide interest in the development of enhanced accident tolerant fuel cladding materials. The aim is to enhance the safety of light water reactors in hypothetical accidental but also in normal operation conditions, by reducing the oxidation rate of the claddings. The claddings are currently made of zirconium-based alloys. Besides the rather long-term concepts (*e.g.*, SiC-SiC ceramic composite), coated Zr-based materials are likely one of the most promising short-term solutions [1, 2].

Among different types of coatings, metallic chromium coatings appear to be the most encouraging candidates [3, 4]. It has been shown that a Cr coating thickness of a few microns to a few tens of microns, deposited on the ∼600 Âţm-thick Zr-based alloy substrate using an optimized process, can reduce significantly the oxidation rate of the cladding under both in-reactor normal operation (∼350ÂřC in water) and accidental conditions (steam at high temperature, *i.e.* above 800ÂřC typically) [5, 6, 7, 8].

The mechanical integrity of the Cr coating is an important issue. However, industrial bulk Cr is relatively brittle at low temperature [9]. Its Ductile-Brittle Transition Temperature (DBTT) is typically between room temperature and 200ÂřC, depending on the material microstructure and the impurities contents in particular. On the one hand, its brittleness can be favoured by a decrease in grain size [10] and the presence of impurities such as nitrogen and carbon [11, 12]. On the other hand, the sensitivity to impurities is greater for recrystallized chromium [13] so that recrystallization can reduce the ductility of chromium. Chromium can show some ductility at room temperature if high purity is ensured [13, 14], or as a result of a plastic pre-deformation beyond the DBTT [12, 15] or with the addition of certain chemical elements [16], which increase the density of dislocations in the material. Nevertheless, one can expect the mechanical behavior of a thin Cr coating to be different from that of a bulk material due to specific grain size, texture or purity, or to thin film effects [17]. As a consequence, the relatively few data available in the literature on the mechanical behavior of bulk chromium cannot be directly transposed to the case of interest here. It is therefore important to characterize the coating as deposited on its substrate.

*Corresponding author.
Email address: Lionel.GELEBART@cea.fr

	%Sn	%Nb	%Fe	%Cr	%O
Zircaloy-4	1.3	<0.005	0.22	0.11	0.13
$M5_{Framatome}$	<0.005	1.0	<0.01	<0.005	0.12-0.14

Table 1
Chemical composition in mass fraction of the Zircaloy-4 et $M5_{Framatome}$ alloys used as substrates.

Stresses are generated in the coating during deposition (residual stresses) or under external loading. When stresses are large enough, different modes of failure may arise depending on the stress state, the quality of the interface with the substrate and the mechanical behavior of the coating (and the substrate) [18]. Data on the mechanical behavior of Cr coatings are very scarce in the literature [19, 20, 21]. They were obtained on coatings deposited using deposition processes different from the one used in this paper, with different thicknesses, on different Zr-based substrates. These data should therefore not be directly applicable to the case studied here. Moreover, under conditions of use, the cladding tube is subjected to mechanical loadings that can be biaxial, along its axial and circumferential directions [22, 23]. Thus, it is important to study the mechanical behavior of the coating as a function of the stress state.

In this paper, the mechanical behavior (*i.e.* damage, plasticity) of a ∼15 Âţm-thick coating deposited on a Zr-based substrate using a particular physical vapor deposition-type process is experimentally investigated at room temperature. This coating is developed in the framework of the French joint research program between CEA, Framatome and EDF. Note that at this temperature, chromiumâĂŹs ductility is expected to be limited whereas the Zr-based alloy substrate is ductile and shows a Young's modulus (∼92 GPa) approximately three times smaller than chromium (∼290 GPa) [24]. The following points are investigated:

– effect of the coating on the overall mechanical behaviour of the cladding,
– coating's failure mode (ductile or brittle) and mechanisms,
– coating's adherence to the substrate,
– initiation and evolution of strain induced coating's damage,
– coatingâĂŹs plasticity,
– effect of loading biaxiality.

For these purposes, biaxial tests and *in situ* uniaxial tensile tests in a Scanning Electron Microscope (SEM) were carried out. They were associated with Digital Image Correlation (DIC) and Acoustic Emission (AE) measurements. The materials and the experimental procedures used are described in Section 2. The results are presented in Section 3 and then discussed in Section 4.

2. Materials and methods

2.1. Materials

The Cr coating is deposited on the outer surface of 50 cm-long tubular cladding segments (9.5 mm outer diameter and 0.57 mm thickness) and on both surfaces of 60x14x1.2 mm^3 sheet samples made of fully recrystallized $M5_{Framatome}$ zirconium alloy. Only one sheet sample with a cold-worked and stress-relieved Zircaloy-4 substrate is used for the Electron Back-Scatter Diffraction (EBSD) analysis described in Section 2.3. The chemical composition of the substrate materials is detailed in Table 1. The substrate surface is not mechanically polished before the deposition. The coating is deposited using an optimized hybrid Direct-Current/High Power Impulse Magnetron Sputtering (DC/HiPIMS) physical vapor deposition (PVD) process [25]. The samples are rotated inside the vacuum chamber during the process in order to ensure homogenous deposition. During the process, the temperature of the substrate is limited (below 250 ÂřC typically) in order not to change its as-received properties.

After the deposition, the coating thickness is measured by X-ray fluorescence at several locations along the samples. Sections where the coating thickness is rather homogeneous with a thickness between 15 and 18 Âţm are then cut from the tubes for the mechanical tests. The coating thickness is quite homogeneous (±0.5 Âţm variations) around the tube circumference. Regarding sheet samples, the coating thickness is rather uniform between 16 and 16.5 Âţm on both main surfaces.

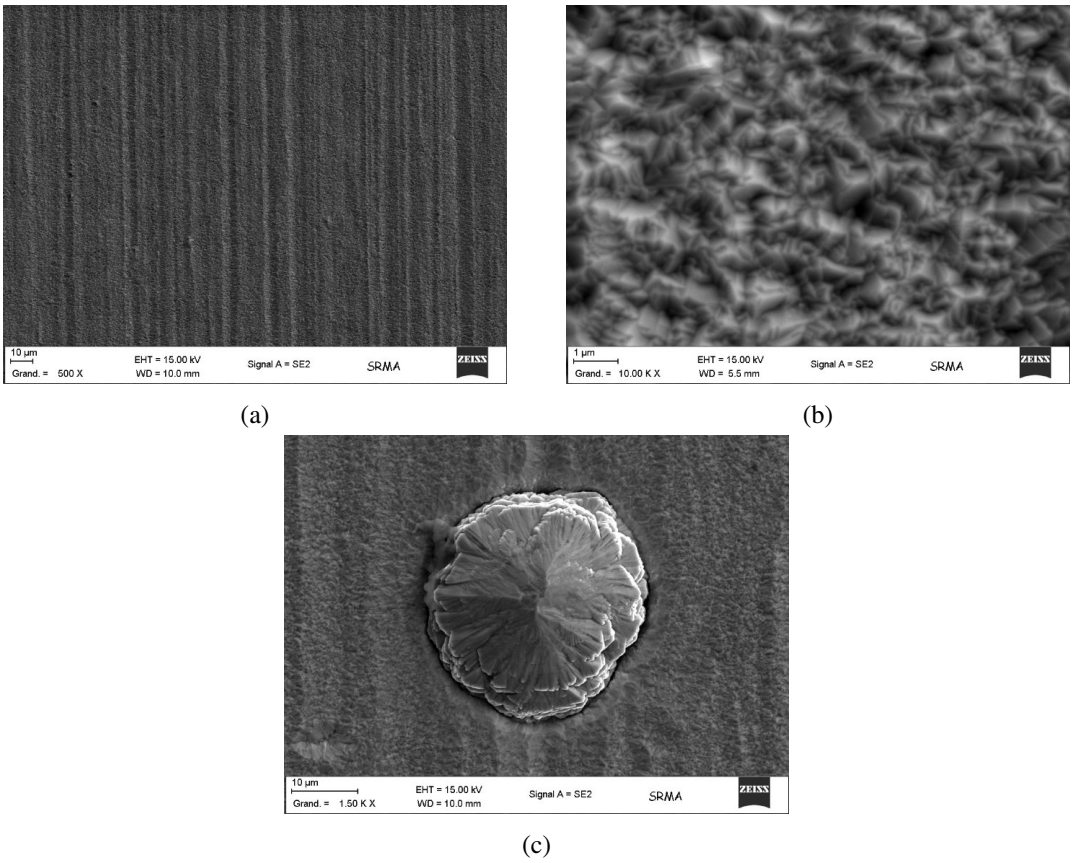

Figure 1: SEM images (secondary electrons) of the Cr coating surface (sheet sample): (a) parallel ridges, (b) pyramid-shaped reliefs and (c) defect.

The morphology and the roughness of the coating surface have been investigated by SEM observation (ZEISS Sigma HD, field emission SEM) (Fig. 1) and by contact roughness measurement (MarTalk device, 2 Âţm-radius 90Âř probe). The surface shows memory from the substrate surface with parallel ridges oriented along the Rolling Direction (RD) on sheets (Fig. 1a) and along the Transverse Direction (TD), *i.e.* the circumferential direction, on tubes. A surface roughness R_a of 0.1±0.02 Âţm along RD and 0.3±0.05 Âţm along TD is measured. The surface roughness of the coating is thus comparable to that of the non-coated substrate. Other deposition processes like cold-spray for example [26], can lead to a surface roughness very different from the one of the substrate. At higher magnification, the surface of the coating exhibits pyramid-like reliefs whose diameter (1-2 Âţm) is comparable to the width of the chromium columnar grains (Fig. 1b). Thus, these reliefs can be associated with the emergence of chromium grains at the outer surface. Furthermore, some local nodular defects (Fig. 1c) are observed in the coating. They have a size of a few micrometers to a few tens of micrometers, and an apex a few micrometers higher than the average surface of the coating. They result from the inhomogeneous growth of the coating likely caused by foreign microparticles during the deposition. Their potential effect on the coating fracture is discussed in Section 3.

Before mechanical testing, the microstructure and crystallographic texture of the coating have been characterized by EBSD analysis. Fig. 2 shows the result of an EBSD scan revealing the microstructure of the coating. The coating is fully dense without evidence of cracks/porosity through the entire thickness or at the coating/substrate interface. The coating microstructure is constituted of columnar grains elongated along the Normal Direction (ND). The grain width is about a few microns near the free surface and a few hundreds of nanometers near the interface. It has been shown that the substrate/coating interface is (semi-)coherent from a crystallographic point of view [27]. Fig. 3 displays the pole figure constructed from EBSD analysis performed on 30x22 Âţm^2 of the free surface of the Cr coating deposited on a $M5_{Framatome}$ sheet sample. The Cr coating exhibits a strong [100] fiber crystallographic texture normal to the surface. The [110] and [111] components which have been often observed for Cr coatings are not observed here likely due to the specific deposition process and parameters [28, 29, 30].

The average residual stresses in the coating have been evaluated by X-ray diffraction performed on coated sheet

samples on the DiffAbs (Diffraction and Absorption) beamline of the SOLEIL synchrotron (France). The analyses were carried out in reflection mode with an energy of the X-ray beam fixed to 18.7 keV so that the penetration depth is larger than the coating thickness. The results are thus average measurements over the whole coating thickness. As a first approach, the internal stresses have been estimated using the $\sin^2\psi$ method. The $\sin^2\psi$ diagrams show a "snake-like" pattern apparently due to the coating crystallographic texture so that only a "semi-quantitative" estimate can be made from the fitted slope. It is beyond the scope of this paper to discuss the relevance of this approach in the present case. Average compressive residual stresses of about 200-300 MPa are estimated in the coating. These stresses are likely mainly related to the highly energetic deposition process (DC/HiPIMS).

Note that the coatings deposited on Zircaloy-4 and $M5_{Framatome}$ substrates show close microstructure, texture and residual stresses.

2.2. Biaxial tests

Biaxial tests are performed on the coated cladding tubes using a servo-hydraulic testing machine (already used in [31]). It consists in applying simultaneously a tensile force and an internal pressure while maintaining constant a stress biaxiality ratio α defined as $\alpha = \sigma_{zz}/\sigma_{\theta\theta}$. The mean nominal axial σ_{zz} and hoop $\sigma_{\theta\theta}$ stresses are calculated as follows:

$$\sigma_{zz} = \frac{PS_i + F}{S} \qquad \sigma_{\theta\theta} = P\frac{\phi - 2e}{2e}$$

where P is the internal pressure and F is the axial force. ϕ and e are respectively the tube initial outer diameter and thickness, measured before testing by laser-scanning (BETA LaserMike, measuring accuracy of approximately 1 Âţm). S_i and S are respectively the initial inner and solid cross section of the tube perpendicular to its axis, calculated as follows :

$$S_i = \pi(\phi - 2e)^2/4 \qquad S = \pi\phi^2/4 - S_i$$

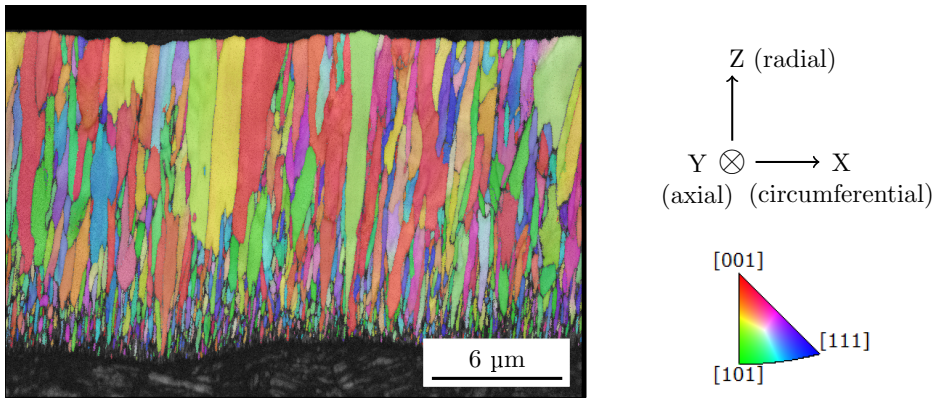

Figure 2: Inverse pole figure 2D map of the crystalline orientation relative to the tube axial direction obtained from cross-sectional EBSD analysis in the thickness of the Cr coating deposited on the outer surface of a $M5_{Framatome}$ cladding tube (35nm/pixel).

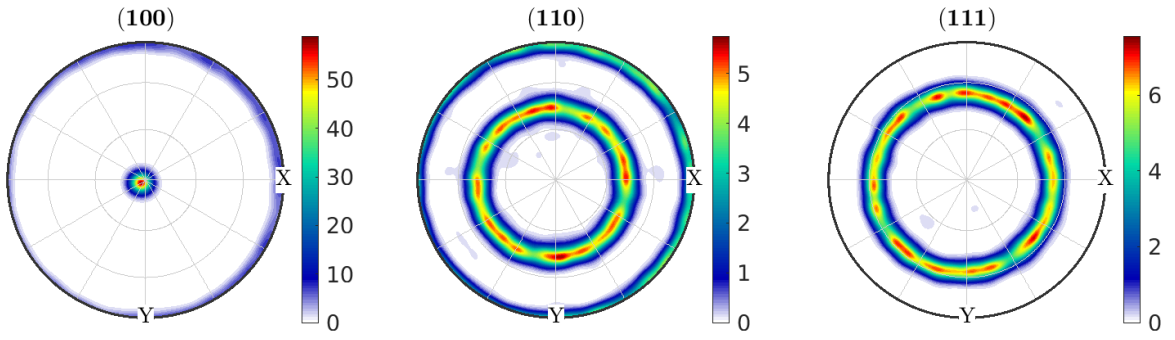

Figure 3: Pole figures constructed from EBSD analysis performed on the free surface of the Cr coating deposited on a $M5_{Framatome}$ sheet sample (X: rolling direction, Y: transverse direction).

Five different biaxiality ratios are tested: ∞ (axial tension, no pressure), 2, 1 (biaxial tension), 0.5 and 0 (circumferential tension, no axial stress). The samples are fabricated from 12.5 mm-long tubes (Fig. 4). Two conical Zircaloy-4 endcaps are electron beam welded at the samples extremities as part of the grip system. Pressurized oil is injected via a hole through one of the two endcaps.

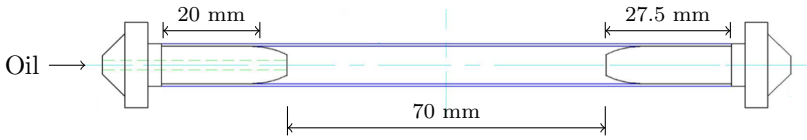

Figure 4: Sample geometry for biaxial tests.

Nominal axial and hoop strains are calculated as follows from the axial displacement ΔL and the radial displacement $\Delta\phi$ measured by axial and radial contact extensometers (Fig. 5) :

$$\varepsilon_{zz} = \frac{\Delta L}{L} \qquad \varepsilon_{\theta\theta} = \frac{\Delta\phi}{\phi}$$

where $L = 50$ mm is the gauge length of the axial extensometer. The radial extensometer is mounted in the middle of the sample. The tests are controlled with a constant strain rate of 2 x 10^{-4} s^{-1} applied on the axial strain in cases where $\alpha = \infty$ and 2 and on the hoop strain in cases where $\alpha = 1$, 0.5 and 0. Maximum applied strain is 5%.

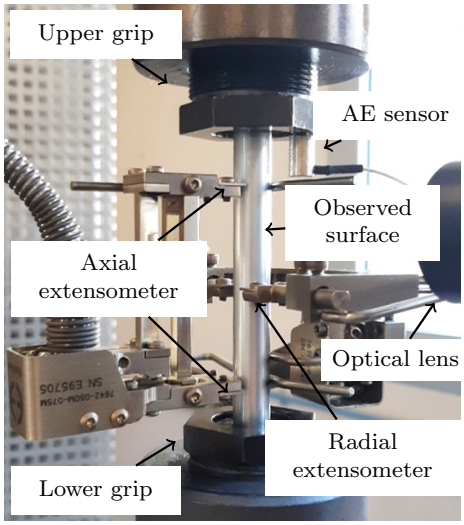

Figure 5: Biaxial testing setup.

During the tests, local strain field at the Cr coating surface is measured by DIC. For this purpose, high resolution 16-bit grayscale images (1600x2160 pixels, 1.625 Âţm/pixels) of the coating surface are acquired using a low noise camera (PCO.Edge 5.5 sCMOS) coupled with a x4 bi-telecentric lens (Opto Engineering TC4M04). The use of a telecentric lens eliminates the dependence of magnification upon the object-lens distance. The natural contrast of the coating surface is used. Indeed, it is sufficient for DIC and appropriate with respect to the target spatial resolution. Furthermore, an artifical speckle may conceal the cracks underneath. The acquisition rate is 10 images per second. The observed surface is enlighten by two halogen lamps. Fig. 6 shows a typical image. The ~2 mm-wide central part of the images is exploited for DIC. Indeed, due to the tabular geometry and the shiny aspect of the Cr coating, it is impossible to obtain an even illumination of the field of view. Because this ~2 mm width is small compared to the tube diameter, the observed surface is nearly flat. Thus, curvature is neglected and local strains are measured by conventional 2D DIC. The CorrelManuV code [32] is used. It relies on a local approach that consists in optimizing the local transformations of independant small correlation domains.

A preliminary study was made to choose the optimal size of the correlation domains (subsets) and to evaluate the measurement uncertainties. It consists in acquiring images of the surface of a specimen placed in the test configuration

by applying a rigid body motion of a few hundred pixels. In this case, zero correlation coefficients and zero strains are expected. The results showed that a size of 30x30 pixels (~32x32 Âţm^2) (Fig. 7) offers the best compromise between precision and spatial resolution of the measurement. Zero-order transformations (pure translations) are used for DIC. This choice is acceptable since the measured strains (<2%) and the size of the correlation domains are small. Finally, a bilinear interpolation is chosen. This interpolation method seems to reduce the amplitude of systematic errors related to the sub-pixel part of the displacements (maximum at 0.2 and 0.8 pixels) [33].

Only the images acquired during the first 100 seconds of the tests, during which the maximum strain remains less than ~1-2%, are exploited, to ensure that the error due to the variation of the distance between the sample surface and the lens remains low (the lens field depth is 0.1 mm). This strain level proves to be sufficient for the objectives of the study insofar as cracking saturation occurs before, as shown in the following. The error on average strain is estimated to be about 0.01%.

Beside DIC, coating cracking is also detected by AE measurement. For this, an AE acquisition system (Vallen AMSY-6) connected to a sensor (VS700-D) and a +34 dB pre-amplifier are used. The sensor is mounted on the upper grip (Fig. 5). Acoustic burst signals whose amplitude exceeds a certain threshold are recorded during the tests, as well as the energy of each recorded event. The threshold (65 dB) is determined as 6-10 dB higher than the maximum acoustic amplitude measured during the same tests performed on uncoated tubes so that all recorded burst signals can be related to coating cracking. To confirm this, experiments performed on uncoated specimens did not exhibit any acoustic emission during the tests.

After testing, the specimens are observed using a 3D optical microscope (KEYENCE VHX-2000F series) at x400 magnification. To statistically evaluate crack density, images covering a large area are recorded so that a sufficient number of cracks is captured. For biaxiality ratios of ∞, 2 and 1, images of 620x10000 Âţm^2 are recorded, by scanning the surface of the tube along its axial direction at two opposite azimuths. For biaxiality ratios of 0 and 0.5, a rotation system is set up to observe the sample surface over a complete circumference, on zones of 830 Âţm in width. The average crack density is calculated as the ratio between the total length of the observed cracks and the area of the observed surface (measured in the deformed configuration).

In addition, in order to observe the interface between the coating and the substrate, and the possible propagation of cracks in the substrate, the tested tubes are carefully cut using a diamond wire then cold resin mounted. In order to preserve the coating state during polishing, a nickel layer is deposited on the coating surface before mounting.

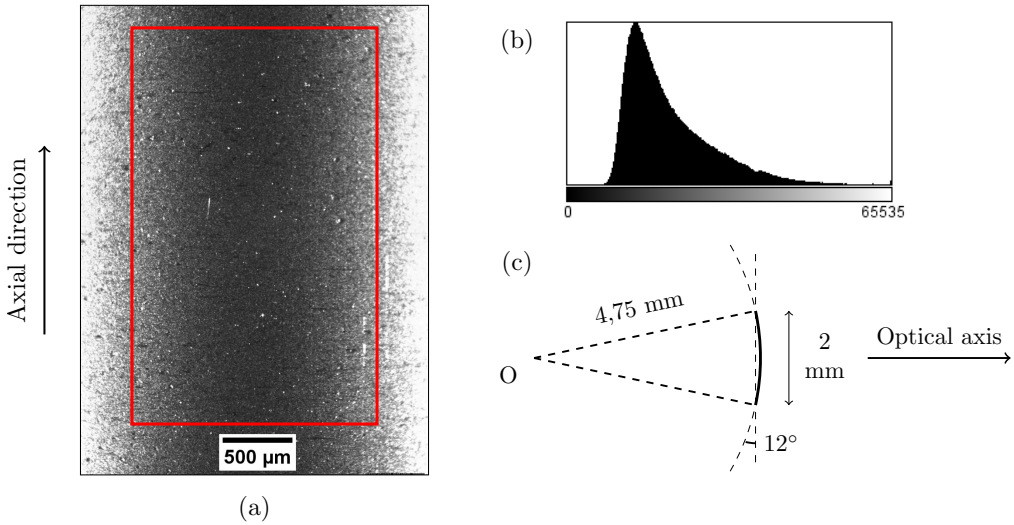

Figure 6: (a) Typical image acquired during biaxial tests, (b) grayscale histogram of the exploited zone (inside red frame in Fig. (a)) and (c) illustration of the observed surface relative to the tube geometry.

2.3. *In situ* tensile test in SEM

In situ tensile tests are performed on dog bone samples (Fig. 8) cut from coated plates by wire electrical discharge machining. Overheating and impact on coating surface are reduced as much as possible during the machining process. In order to enhance the contrast for DIC, two 100x100 Âţm^2 micro-grids made of organometallic compounds of Pt

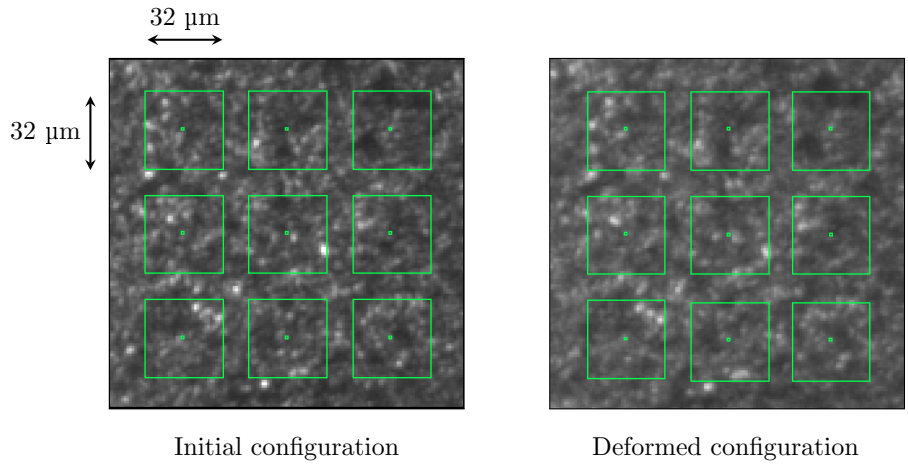

Figure 7: Typical subsets used for DIC for biaxial tests in the initial configuration and for 2% mean axial strain (only one subset out of four is shown).

(grid nÂř1) and of W (grid nÂř2) are deposited on the coating surface by Focused Ion Beam (FIB) using a FEI HeliosNanoLab 650 SEM. The grids have a step size of ∼1 Âţm and a line thickness of ∼300 nm.

The tests are carried out at room temperature inside a SEM equipped with a tungsten filament (JSM-IT300 JEOL), using a micro tensile testing machine (Proxima model from microMECHA, 3 kN load cell). A small preload (50N) is applied after sample mounting to garantee proper alignment. The loading is applied by controlled displacement with a constant rate of 2 Âţm/s corresponding approximately to a strain rate of 10^{-4} s^{-1}. The tests are interrupted (zero displacement increment) 10 times at different loading levels in order to capture the initiation and evolution of coating cracking via SEM observation.

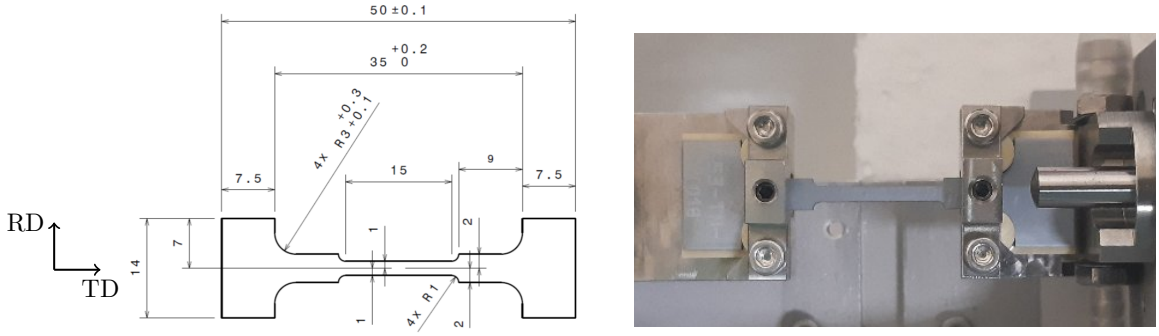

Figure 8: (a) Sample geometry (1.2 mm-thick) for the *in situ* tensile test in SEM (unit: mm) and (b) sample mounted.

The observations are made with an accelerating voltage of 20 kV. A working distance of 17.2 mm is chosen, so that the sample surface is relatively close to the electron gun to have a good resolution, while avoiding any collision with the testing device. The opening of the diaphragm and the beam current are chosen by trying to minimize the spurious strains measured by DIC on two images of the grid 1, following a rigid body motion of the stage (and the specimen).

At each interruption, crack density is evaluated over a length of 4 mm along the loading direction located between two existing defects on the coating. A high magnification (x22000) SEM image of each counted crack is taken at the centerline of the sample width at each interruption for crack opening measurement. The lips of the cracks are detected by locating an abrupt change in the gray level on a line parallel to the loading direction (Fig. 9). Crack opening is measured with an uncertainty of ∼150 nm. The opening of each crack and the corresponding uncertainty are derived from measurements made on 10 equidistant lines (spaced 0.4 Âţm apart) in each image.

The mean nominal stress is determined from the ratio between the applied force and the initial gauge section of

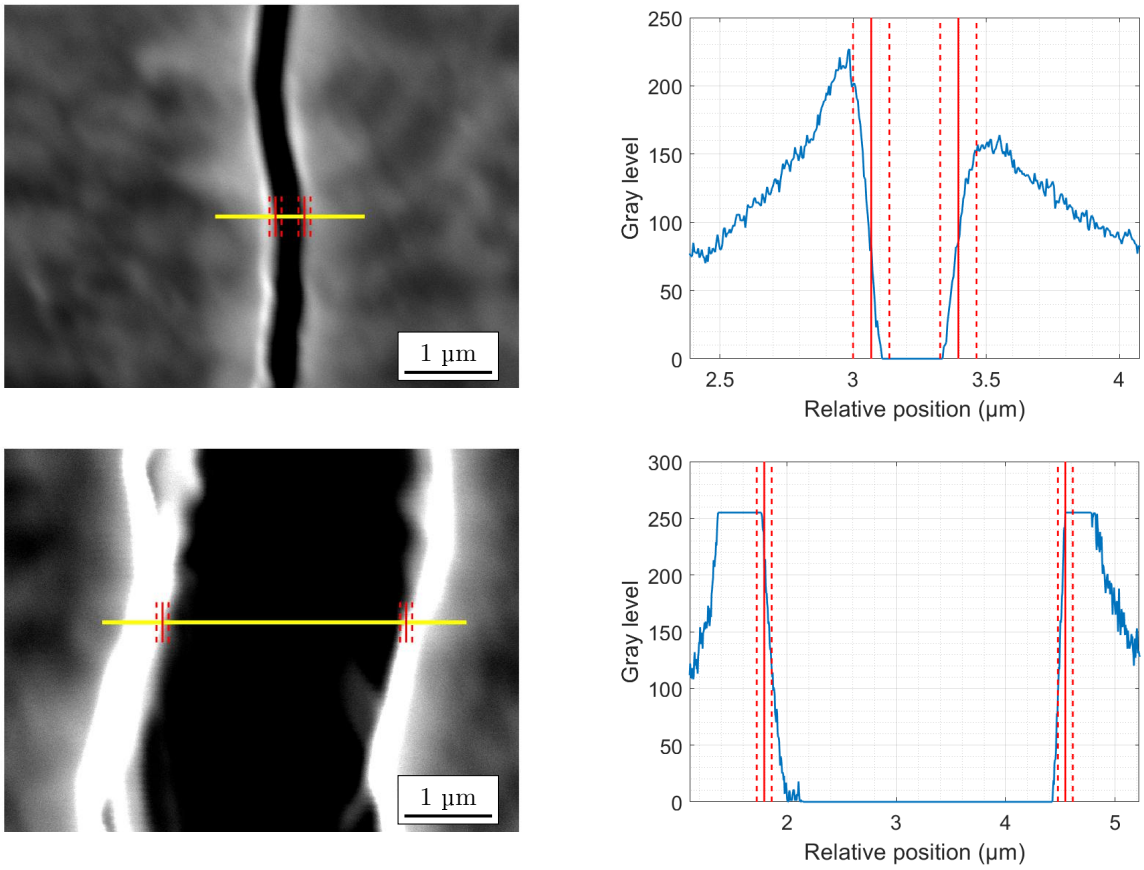

Figure 9: Illustration of crack opening measurement from SEM images in secondary electron mode at x22000 magnification (the measurement uncertainty is illustrated by the vertical dashed lines on the right figure).

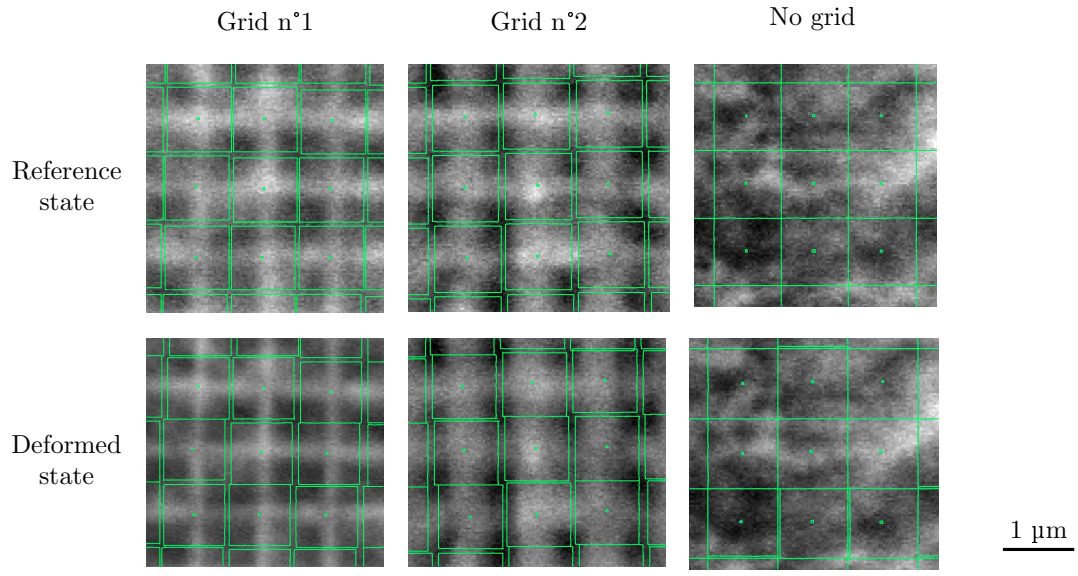

Figure 10: Typical subsets used for DIC for *in situ* tensile test in SEM, in the reference and deformed configurations, in grid 1, grid 2 and no grid regions.

the specimen (coating thickness included). The macroscopic strain is indirectly calculated by supposing that all the plastic displacement evaluated from the force-displacement curve originates from the plastic strain of the specimen gauge length. More precisely, it is calculated by adding the elastic strain, calculated from the nominal stress and the

known YoungâĂŹs modulus of the Zr alloy substrate (as shown later, the coating does not have a significant effect on the global elastic stiffness of the coated material), and the plastic strain, calculated as the ratio between the plastic displacement and the specimen initial gauge length.

The local strain in the Cr coating is measured by DIC. For this, high resolution 8-bits SEM images (5120x3840 pixels, ∼31 nm/pixels) of the coating surface are acquired in Secondary Electrons (SE) mode before loading and at each interruption. The sample surface altitude is adjusted after each test interruption and before images capture so that the working distance where the images are in focus remains constant (17.2 mm). It is to eliminate artifact in strain measurement induced by magnification change. Fig. 10 shows typical subsets used for DIC. Subsets are centered on the grid junctions (1 Âţm step). A parametric study has been performed to optimize the parameters used for DIC. For that purpose, images were taken before and after having applied a rigid translation of ∼20 Âţm (∼700 pixels). It emerges that a 30x30 pixels (∼1x1 Âţm^2) subset size offers the best compromise between accuracy of the measurement and spatial resolution. Furthermore, the smallest errors are obtained when using a bilinear interpolation. In addition to the images of the microgrids, images of the natural coating surface without any microgrid (which show enough contrast) are recorded. In this case, the subsets (30x30 pixels) are positioned regularly side by side. On average, the level of error in strain measurement by DIC is smaller and less variable where micro-grids have been deposited. The standard deviation on strain obtained after applying the rigid translation is 1.1-1.3% with micro-grids and 1.1-2.9% without.

In order to study the cracking mechanisms, the fracture surface of the coating in the necked region of the specimen after complete failure is observed. In addition, in order to relate crack propagation to the coating microstructure, an EBSD study is carried out in the vicinity of narrow-open channeling cracks (< 100 nm) in a chromium coating deposited on a cold-worked and stress-relieved Zircaloy-4 substrate, cracked during an *in situ* tensile test in SEM. The EBSD analysis is performed using a field emission SEM (ZEISS Sigma HD) directly on the surface of the coating, without any surface preparation which could have changed the state of the rather thin material. Despite non-negligible surface roughness, an indexing rate of about 70% is reached. The EBSD analysis is done in the vicinity of eight ∼20 Âţm-long cracks.

3. Results

3.1. Coating cracking as a function of stress biaxiality

Fig. 11 shows the nominal stress-strain curves obtained for the reference uncoated and the Cr-coated tubes from biaxial tests (the stress values are normalized for the sake of confidentiality). It is shown that the 15-18 Âţm-thick Cr coating has little effect on the macroscopic response of the tubes at room temperature. Cracking of the coating is not visible on the macroscopic response.

The cracks in the coating are visualized by DIC through bands of localization on strain maps as shown in Fig. 12 for the case of axial tension. Each crack appears instantaneously between consecutive images (separated by 0.1 seconds). The evolution of crack density (obtained by dividing the total crack length by the observed area) as a function of the applied strain (up to ∼1-2%, after, the surface moves out of the field depth) determined from these strain fields is shown in Fig. 11. Using this method, the crack density is only measured within a relatively small surface (< 2x3 mm^2) compared to the sample dimension. More global information is obtained using AE. The normalized cumulated acoustic energy captured during the tests is also shown in Fig. 11.

The two approaches (DIC and AE) provide rather consistent results. The Cr coating starts to crack approximately when the substrate starts to yield macroscopically. After the onset of cracking, a sharp increase in crack density is observed. The strain-induced crack densification is then progressively slower until saturation after which no additional crack forms with increasing load.

Table 2 reports the crack onset strains determined along the tube axial and hoop directions for all tested biaxiality ratios. It is shown that the crack onset strain is significantly higher in the case of hoop tension ($\alpha = 0$) than in the case of axial tension ($\alpha = \infty$).

Fig. 13 shows the crack pattern in the coating as observed after testing. Cracks in the coating tend to propagate in a direction normal to the direction of the maximum principal stress applied to the tubes: in the case of biaxiality ratios equal to ∞ and 2, the cracks propagate in the hoop direction; in the case of biaxiality ratios of 0 and 0.5, the cracks propagate rather along the axial direction, although they are slightly inclined and branched in the case of 0.5 biaxiality ratio. In the case of equi-biaxial stress state, cracks propagate in different directions or follow a non-straight trajectory resulting in a mud-crack pattern.

For biaxiality ratios of ∞, 2 and 0, the cracks are not branched and generally parallel to each other. Fig. 14 shows

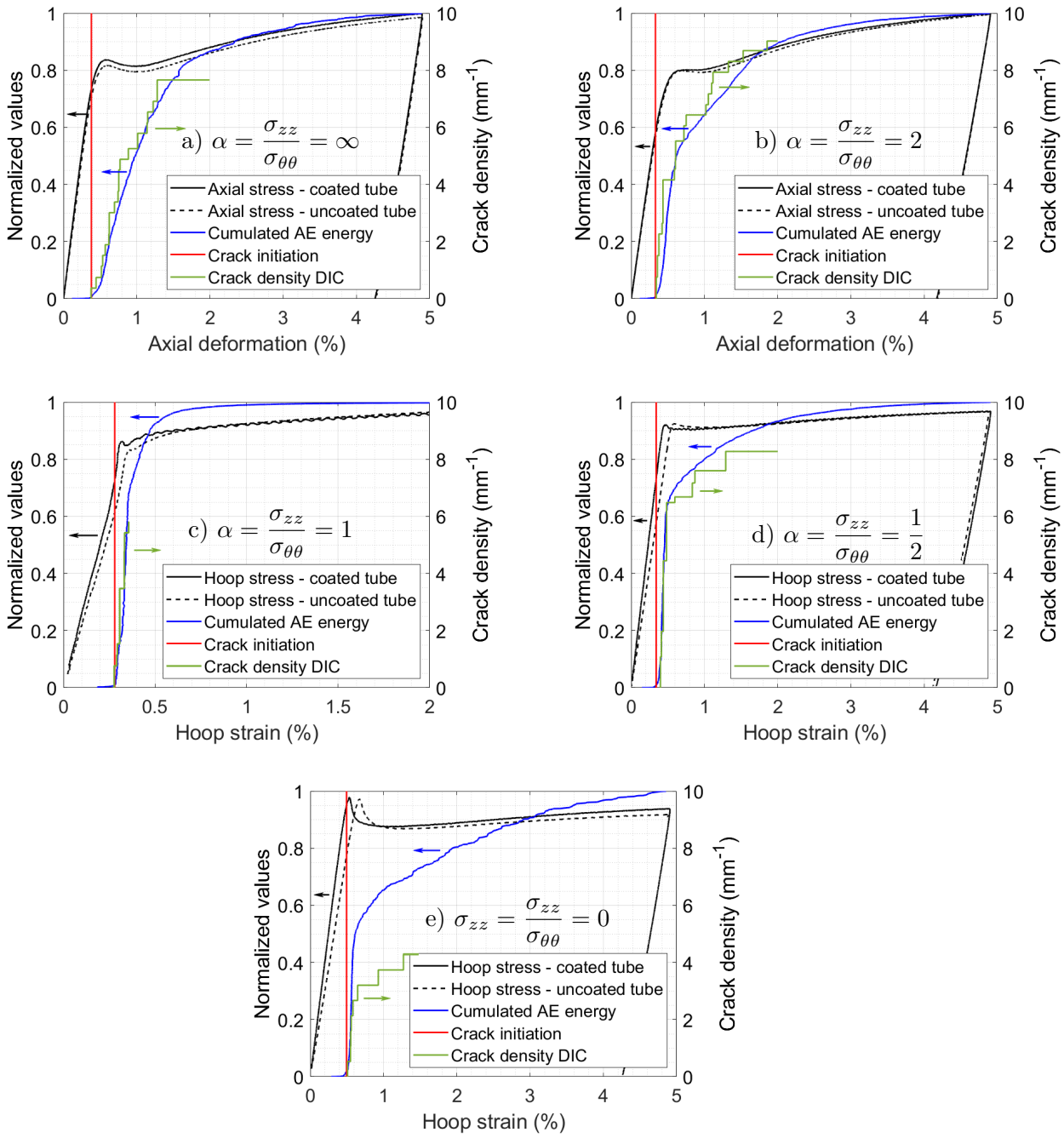

Figure 11: Crack densification determined via DIC and AE in relation to the macroscopic nominal stress-strain curves from biaxial tests on coated (and uncoated) $M5_{Framatome}$ cladding tubes, for stress biaxiality ratios of a) ∞, b) 2, c) 1, d) 0.5 and e) 0. The difference of elastic stiffness observed for stress biaxiality ratios of 1, 0.5 and 0 is due to the indentation of radial extensometers into the tube surface making the measurement incorrect.

histograms of the width of the uncracked regions between cracks at saturation. The size of the uncracked regions at saturation is highly variable for a given sample: the largest regions are about 5-6 times greater than the smallest ones.

In terms of crack length, on the one hand, cracks propagate rather freely in the tube axial direction in the case of hoop tension. Their length usually reaches several centimeters. On the other hand, in the case of axial tension and biaxiality ratio of 2, cracks propagating in the hoop direction rarely cover a complete circumference of the tube. Fig. 15 shows the results of a statistical study on the length of the observed cracks. The length of the cracks is expressed by their angle of propagation according to the tube circumference. In terms of number of cracks, most cracks propagate up to 90Âř around the tube axis. Only a few cracks propagate beyond a full circumference. In terms of cumulative

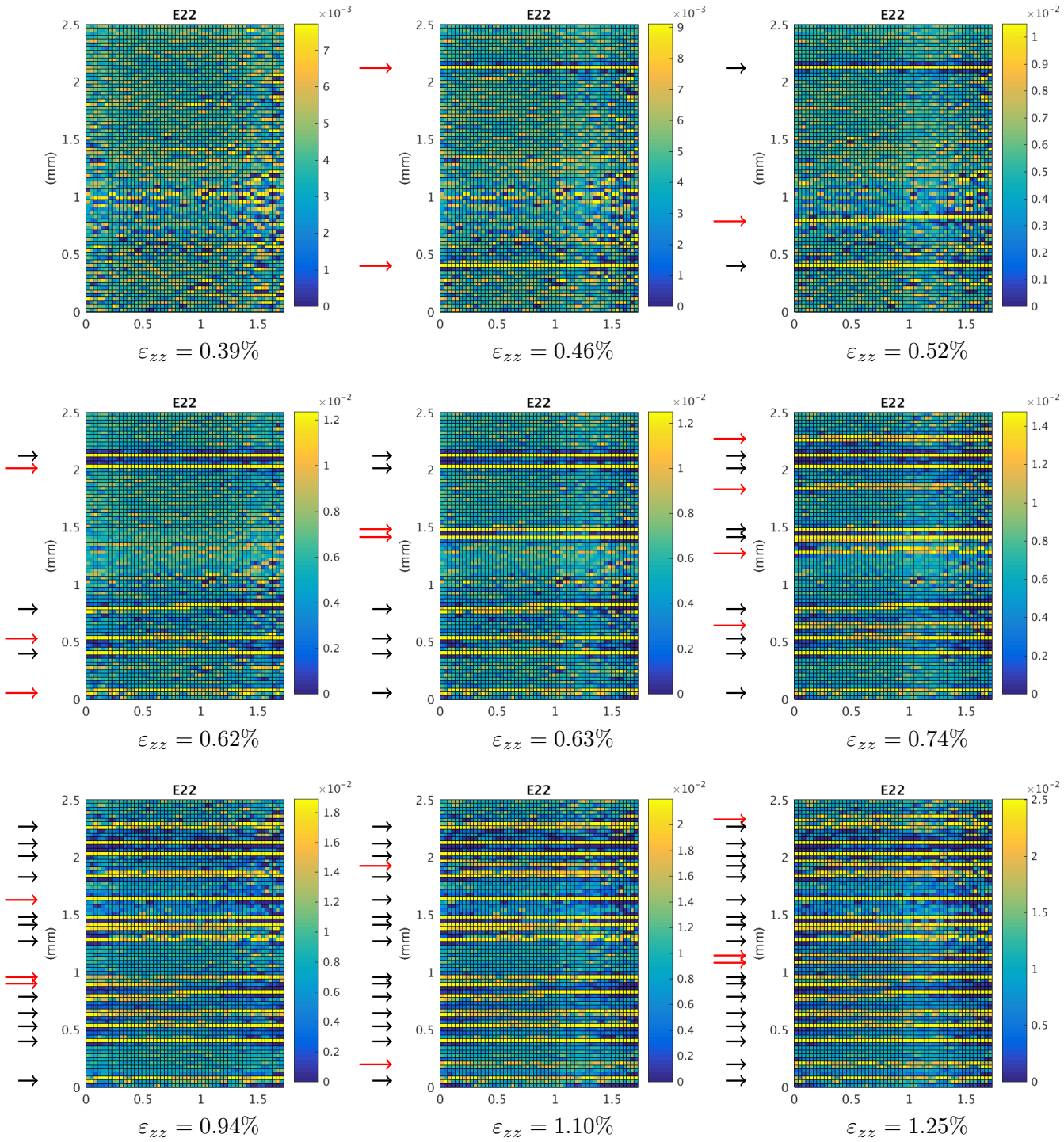

Figure 12: Local (Green-Lagrange) strain map in the tube axial (vertical) direction mesured by DIC at different loading levels on a coated $M5_{Framatome}$ tube subjected to axial tension. Cracks are located by arrows, black and shorter when the crack was already present in the previous step, red and longer when it is new. The average strain values measured in the region of interest are given below the color maps.

length, these cracks propagating over more than one circumference represent a fairly large proportion. Moreover, these long cracks show a helix-shape propagation with a pitch of about 30-100 Âţm, equivalent to an inclination of 0.05 to 0.2Âř with respect to the circumferential direction.

Interactions between the cracks and the few defects in the coating are observed: the crack may cross, propagate under, deviate around or stop at the defect, depending on the case, as shown in Fig. 16.

α	Axial strain (%)	Hoop strain (%)	Axial stress (MPa)	Hoop stress (MPa)	Crack density (1/mm)
∞	0.39 ± 0.01	-0.11 ± 0.01	1115 ± 38	-74 ± 38	8.5
2	0.34 ± 0.01	0.06 ± 0.01	1076 ± 38	441 ± 38	10.6
1	$0.32 \pm 0,01$	0.26 ± 0.01	1150 ± 38	1007 ± 38	18.6
0.5	$0,07 \pm 0.01$	0.33 ± 0.01	435 ± 38	1053 ± 38	11.2
0	-0.21 ± 0.01	0.48 ± 0.01	-318 ± 38	1322 ± 38	5.3

Table 2
Axial and hoop strains and stresses in the Cr coating at the onset of cracking and crack density at saturation for all tested biaxiality ratios (stresses include initial residual stresses and they are estimated assuming plane stress condition and that the coating remains elastic before cracking).

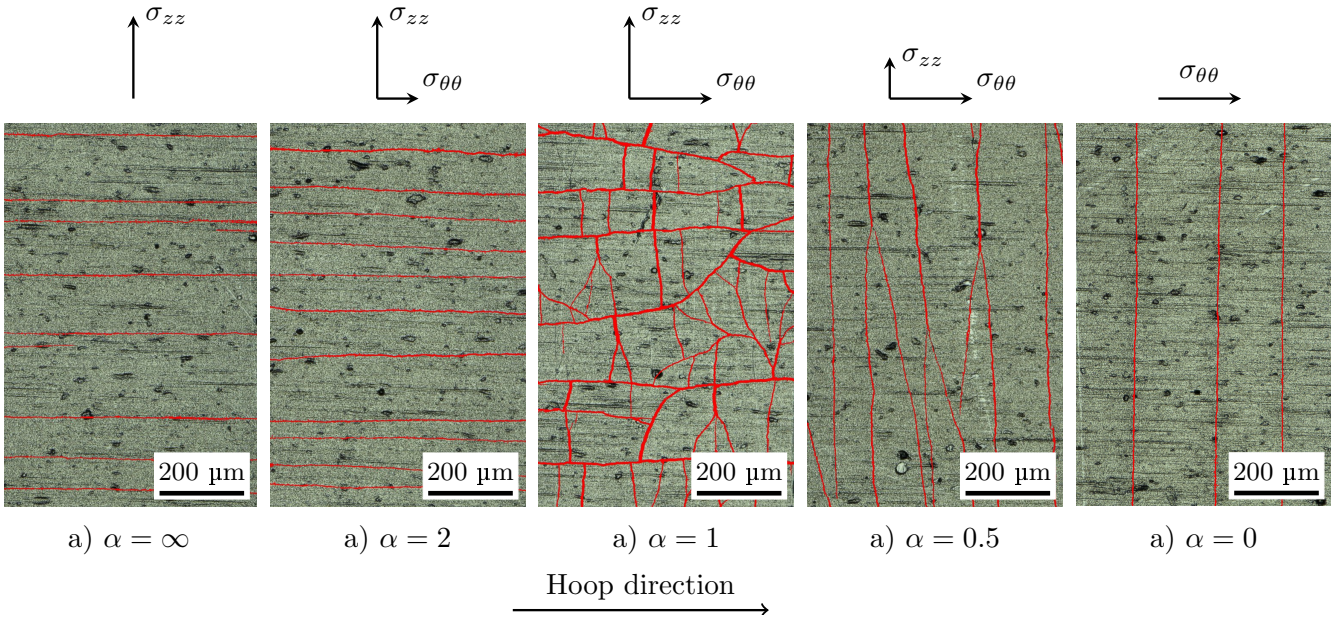

Figure 13: Crack patterns in the coating observed after testing using a 3D optical microscope. Cracks are highlighted in red.

It is observed that the crack density is rather uniform over a 40 mm-long zone in the center of the tubes, where the hoop strain is rather homogeneous according to laser-scanning measurements of the outer diameter performed after testing along the tube axis. The crack density at saturation determined from the observations made over large surfaces are reported in Table 2. The crack density at saturation is greater in the case of axial tension than in the case of hoop tension. The crack density is greater for biaxial loading, in particular in the case of equi-biaxial loading.

Fig. 17 displays the cross-sectional observation of cracks in the coating thickness. Channeling cracks (propagation directions parallel to the coating/substrate interface) propagate through the whole thickness of the coating but do not significantly penetrate into the substrate (for the ~5% maximum macroscopic strain levels applied during the expriments). No debonding of the coating is observed.

3.2. Coating plasticity and cracking on a microscopic scale

Fig. 18a shows the force-displacement curves obtained during *in situ* tensile tests performed in SEM at room temperature on uncoated and Cr-coated $M5_{Framatome}$ samples. The tensile test on the Cr-coated sample was interrupted multiple times. Stress relaxation is observed during the interruptions. The test on the uncoated samples has not been interrupted. Nevertheless, the responses of the coated and uncoated specimens are relatively similar. The difference observed is not *a priori* due to the presence of the coating (as demonstrated in Fig. 11) but rather to the multiple interruptions. Fig. 18b displays conventional macroscopic stresses and strains at each interruption in the gauge length of the sample (15 mm). The last interruption is at about 6% of macroscopic strain.

At each interruption, channeling cracks across the specimen width are observed in the coating (Fig. 19a). These

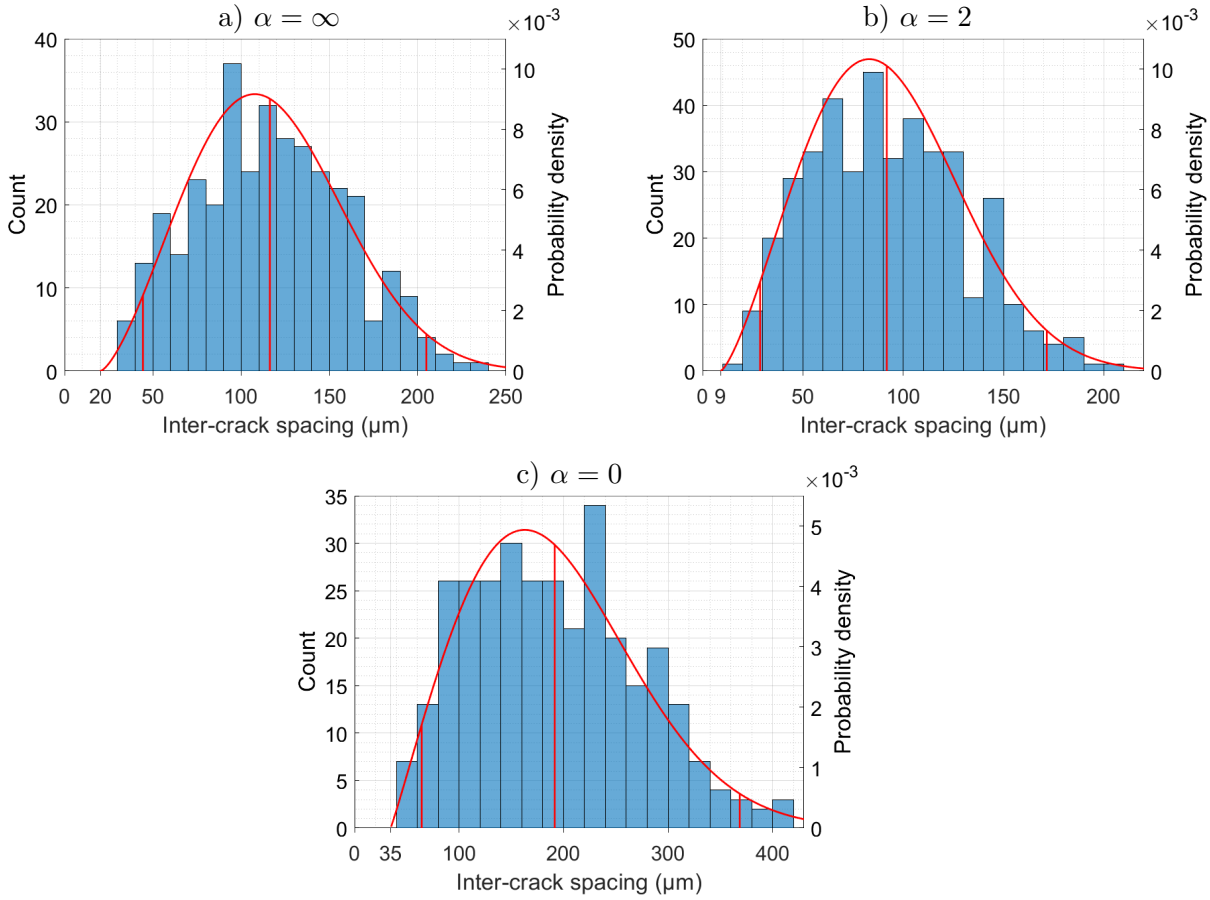

Figure 14: Histogram of the sizes of uncracked regions at saturation for different biaxiality ratios (the mean value and values at 95% of the fitted three-parameter Weibull distribution are represented by red vertical lines).

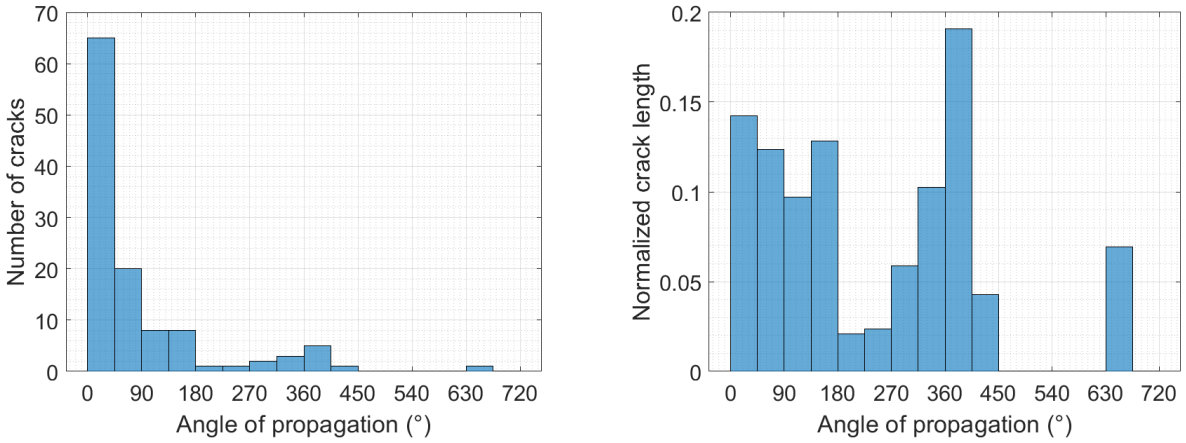

Figure 15: Histogram of the length, expressed in propagation angle, of cracks in the coating propagating in the tube hoop direction during axial tensile test.

cracks initiate from microcracks at the edges of the sample which stem from the machining process. The evolution of crack density as a function of applied strain is shown in Fig. 19b. Only cracks propagated beyond the centerline of the sample width are counted. Those remaining short and confined at the edges are excluded. The microcracks observed at the edges of the specimen prior to the test tend to propagate during the test. However, only some of them completely cross the specimen width. Thus, the density of cracks is greater at the specimen edges than in the middle of the specimen, which is more representative of the case of a coating on a tube (without singularity). In

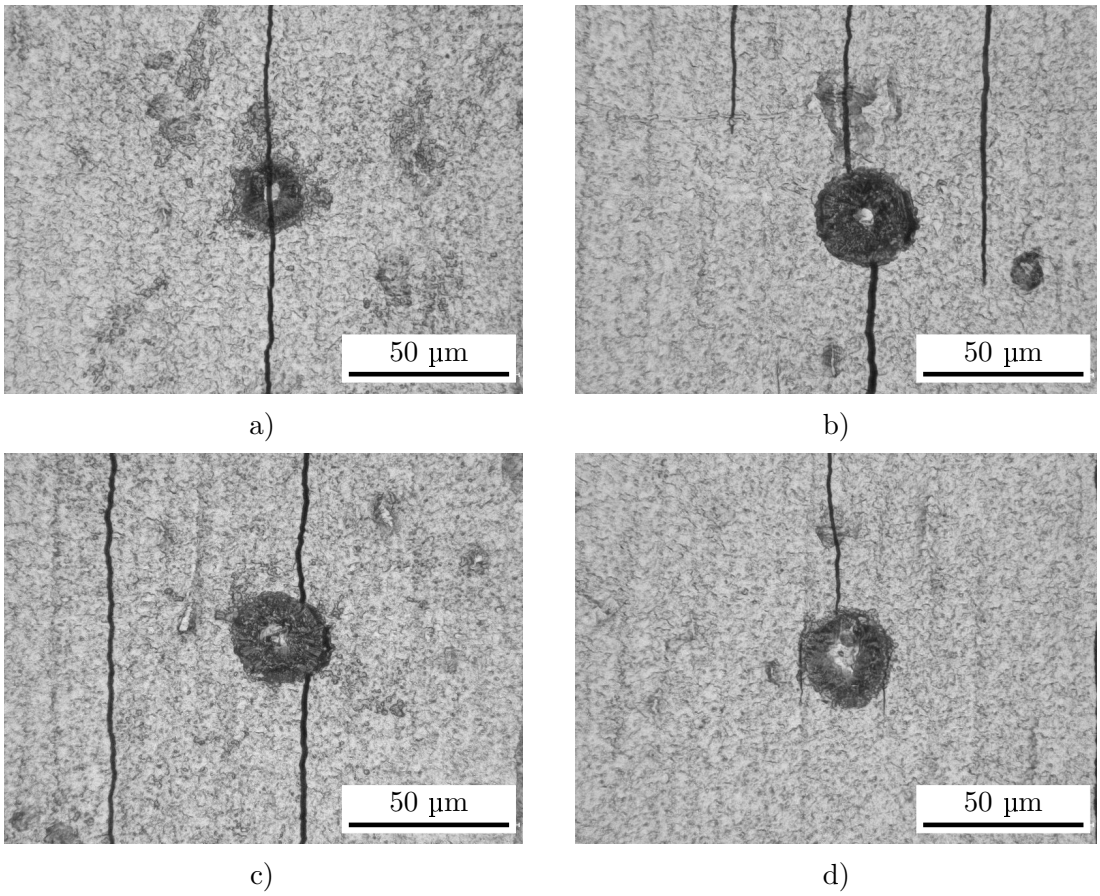

Figure 16: Interaction between cracks and defects in the coating: (a) crossing, (b) propagatation under, (c) deviation around and (d) stopping.

addition, the defects observed in the coating (Fig. 1c) are not crack initiation sites. In some cases, they even stop crack propagation. Incipient cracking of the coating is observed at applied macroscopic strain of about 0.4%. The crack density then strongly increases with applied strain between 0.4% and 1%. Very few new cracks are detected after 1% of macroscopic strain. The crack density at saturation is 9-10 mm^{-1}.

Fig. 20 shows the measured opening of a crack set systematically analyzed after each test interruption. The same curve color was attributed in Fig. 20a to a crack set newly observed after test interruption at a given applied strain. Those observed before and at the fifth interruption are all assigned the blue color. The initial crack opening is about 200 nm. Then, the cracks open regularly with increasing applied strain. At about 6% of macroscopic strain, the crack opening is about 3 Âţm. On average, the strain induced crack opening evolution remains about the same regardless of the macroscopic strain at which the cracks appear (*i.e.* the slopes are very similar). The few cracks observed after cracking saturation at larger applied strain remain less opened compared to the others and contribute little to the overall crack opening.

The contribution of crack opening to macroscopic strain is shown in Fig. 20b. The strain associated with crack opening is defined as the ratio between the sum of the crack openings and the length along which the cracks are measured. It is found that crack opening and intrinsic deformation of the coating both account for approximately 50% of the applied strain. In other words, at 6% of macroscopic strain, the mean strain in the loading direction of the remaining uncracked coating is about 3%.

The local strains measured by DIC on the coating are shown in Fig. 21. A pattern of strain heterogeneity is clearly observed consisting of localization bands oriented at 45Âř with respect to the loading direction. The band length is about 40 Âţm. The band width is in the order of the Cr grain size. This pattern appears from the onset of macroscopic plasticity and remains unchanged with the increasing applied strain.

To visualize the strain distribution between two cracks, the remaining uncracked portion of the coating is divided into strips parallel to the cracks. The mean strain within these strips is then calculated (from DIC measurements).

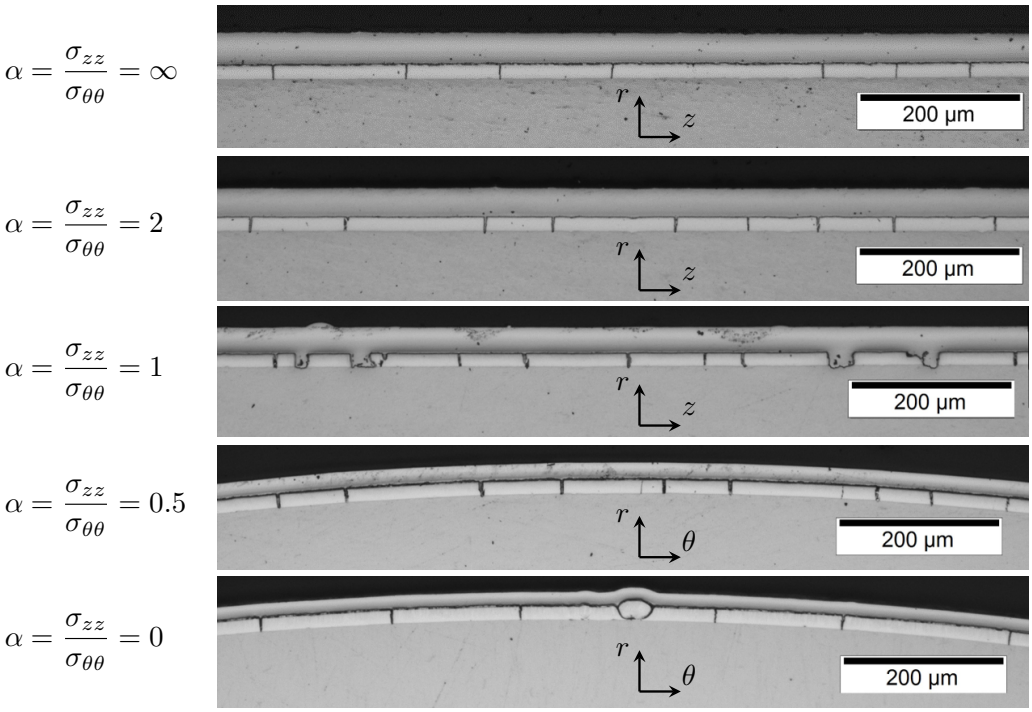

Figure 17: Cross-sectional observation of cracks in the coatings after tests on $M5_{Framatome}$ coated tubes at different stress biaxiality ratios.

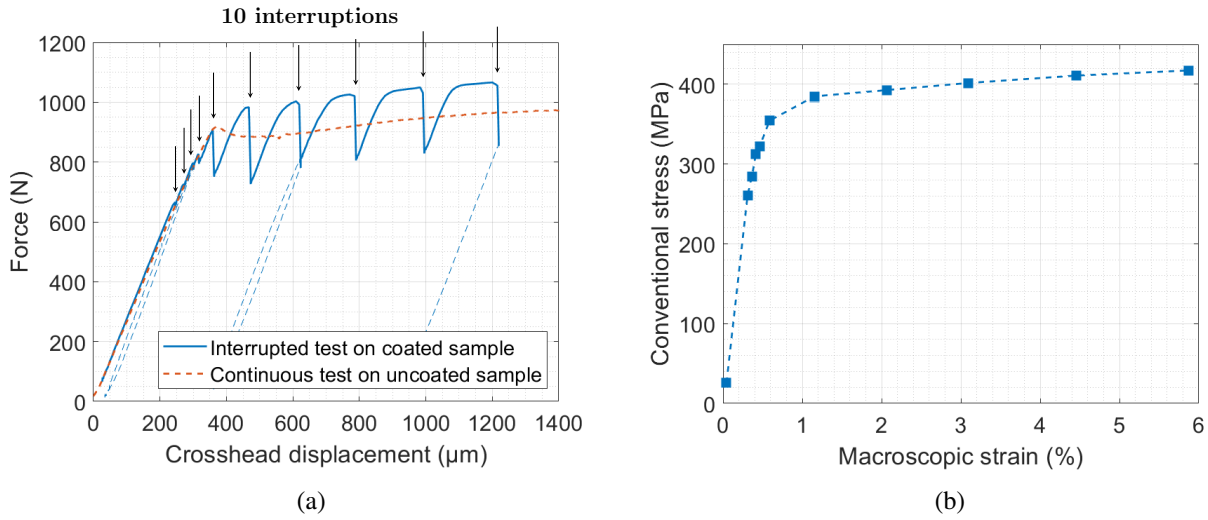

Figure 18: (a) Force-displacement curves obtained during *in situ* tensile tests performed on uncoated and coated $M5_{Framatome}$ sheet samples, (b) conventional stress and macroscopic strain at each interruption during the test performed on the coated sample.

The results are shown in Fig. 21 as strain profile according to the relative position to the cracks for different loading levels. First, it is clear that the coating region near the cracks is less deformed. The coating strain is maximal at mid-length between cracks and its maximum value depends on the distance between cracks. The uncracked coating is less deformed if the intercrack distance is smaller. Second, the uncracked coating is progressively loaded after the cracking saturation, along with the increase of crack opening. At the meso-scale, the coating strain can reach 6% at mid-distance between the cracks, in the order of the applied macroscopic strain. It is even higher locally at a finer scale, up to 10%.

Fig. 22 shows orientation maps of the Cr coating around cracks derived by EBSD. It is found that channeling cracks, or at least their emergence on the coating outer surface, are both intergranular and transgranular in comparable proportions. Fig. 23 shows the misorientation angle between neighboring grains on the two sides of intergranular

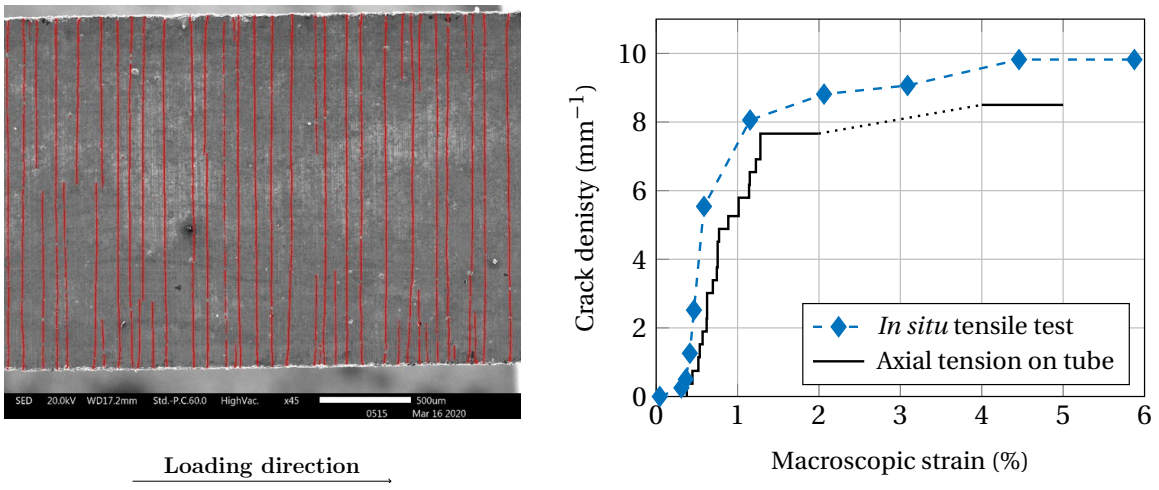

(a) (b)

Figure 19: (a) Crack pattern highlighted in red, (b) evolution of crack density as a function of the macroscopic strain during the *in situ* tensile test inside SEM performed on a coated $M5_{Framatome}$ sheet sample (comparison to the crack density measured during an axial tensile test on a coated tube).

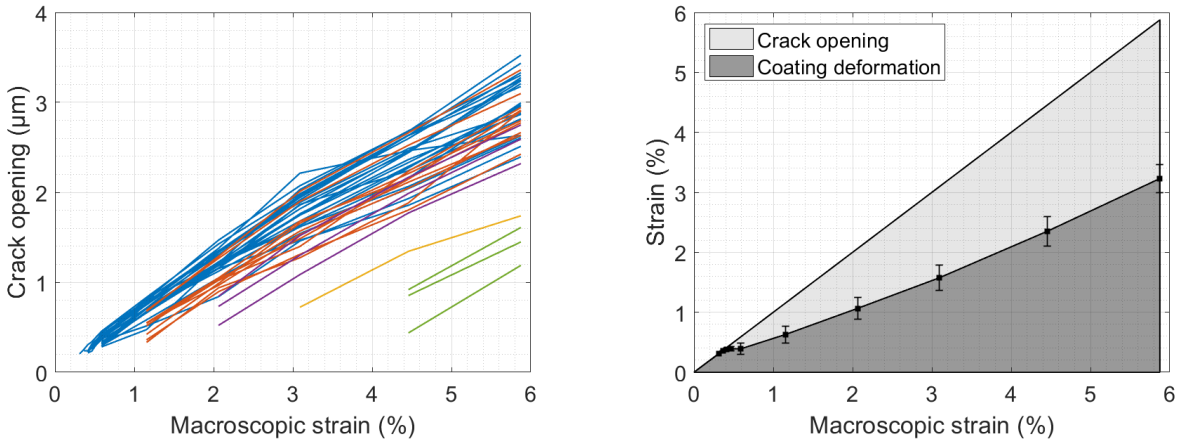

(a) (b)

Figure 20: (a) Evolution of the opening of each crack and (b) contribution of crack opening to the macroscopic strain during the *in situ* tensile test inside SEM on a coated M5Framatome sheet sample.

cracks measured from EBSD data. Intergranular cracks propagate preferentially along grain boundaries with a large angle of disorientation, greater than 20Âř.

Fig. 24 shows the fractography of the coating in the necked region after the total failure of the specimen. Features associated with brittle failures with both cleavage and intergranular decohesion are observed. At higher magnification, the fracture surface exhibits traces of dislocation slip.

4. Discussion

It is shown in Section 3 that there is a minor difference between the uncoated and coated material regarding the macroscopic mechanical behavior. This is consistent with the results reported in [34] for a 5-8 Âţm-thick chromium coating deposited by cathodic arc evaporation on a Zr1Nb substrate.

The defects are not considered as preferential sites for crack initiation as many defects in the coating are not connected to any crack. Moreover, detachment of some growth defects which are on crack propagation path is observed, due to the relatively weak cohesion of the defects with the rest of the coating. This phenomenon can contribute to

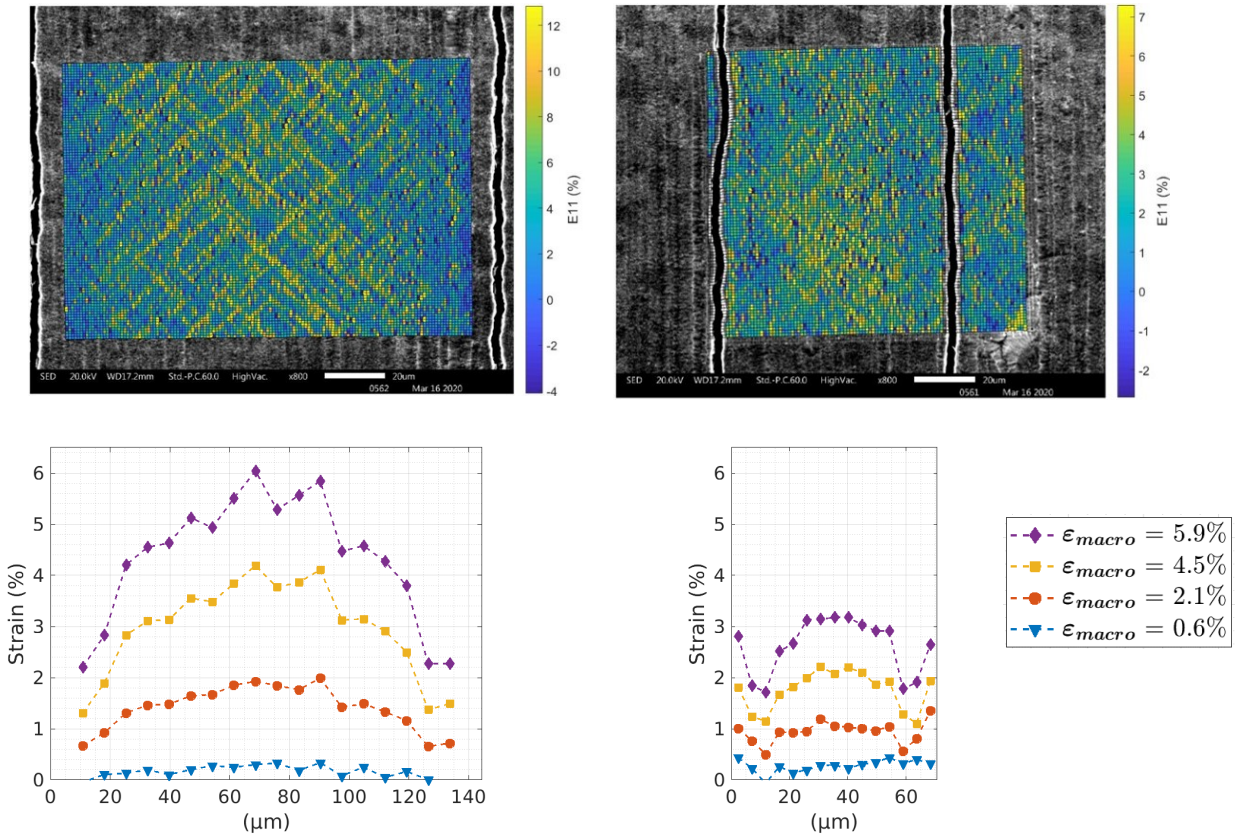

Figure 21: Map of local strain along the loading (horizontal) direction measured by DIC on the Cr coating (sheet sample, $M5_{Framatome}$ substrate) at 6% of macroscopic strain and profile of strain along the loading direction between two cracks at different loading levels.

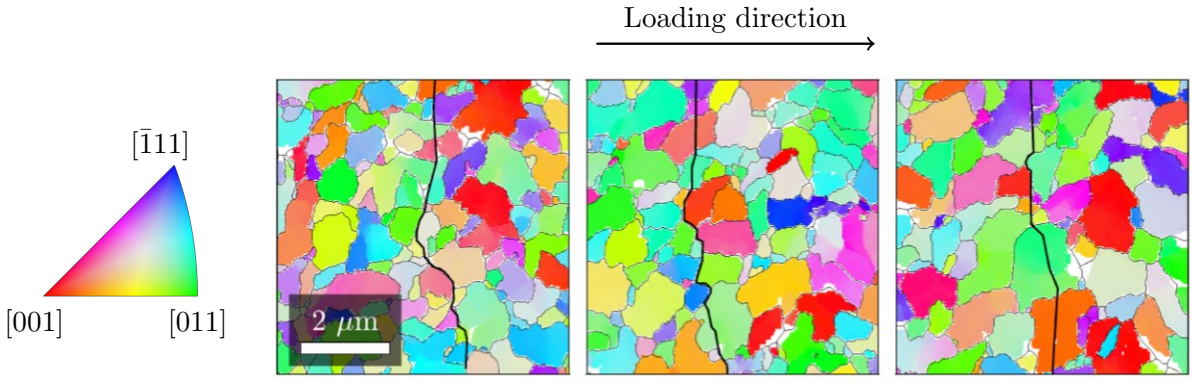

Figure 22: Inverse pole figure EBSD maps (35 nm/pixel) on the two sides of channeling cracks (thick black line) in the coating on a Zircaloy-4 plate sample subjected to uniaxial tension. The color represents the in-plane (loading) direction within the crystal system.

stress relaxation near the crack tip and slow down crack propagation.

Crack onset strains of 0.39% and 0.4% have been measured along the loading direction in the case of axial tension on tube and on plate sample, respectively. A crack onset strain of 0.48% has been obtained along the loading direction in the case of hoop tension on tube. These values are comparable to those reported in the litterature for other Cr coatings, despite difference in substrate, coating thickness and deposition method: 0.41% for a 10 Âţm-thick coating, deposited on a recrystallized Zircaloy-4 sheet substrate using a multi-arc ion plating technique, loaded under uniaxial tension [19]; 0.35-0.45% for a 30-45 Âţm-thick coating deposited by cold spraying on a Zr-based alloy (not specified) tested under 4-point bending and expansion due to compression, generating a predominantly circumferential loading

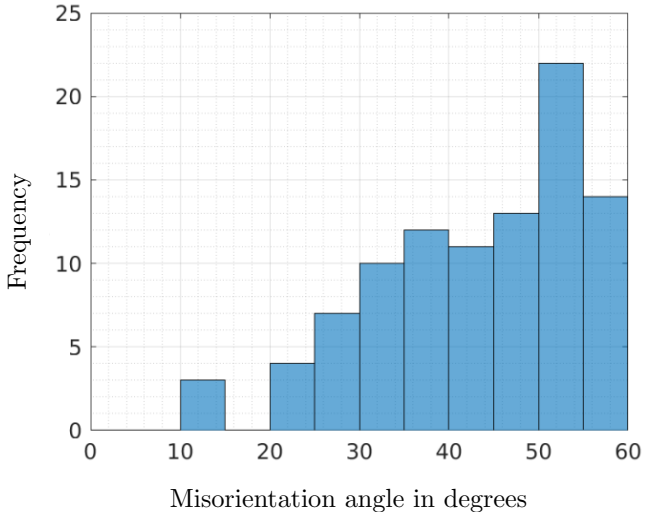

Figure 23: Histogram of misorientation angles between neighboring grains obtained by EBSD on the two sides of intergranular cracks in the coating on a Zircaloy-4 sheet sample subjected to uniaxial tension.

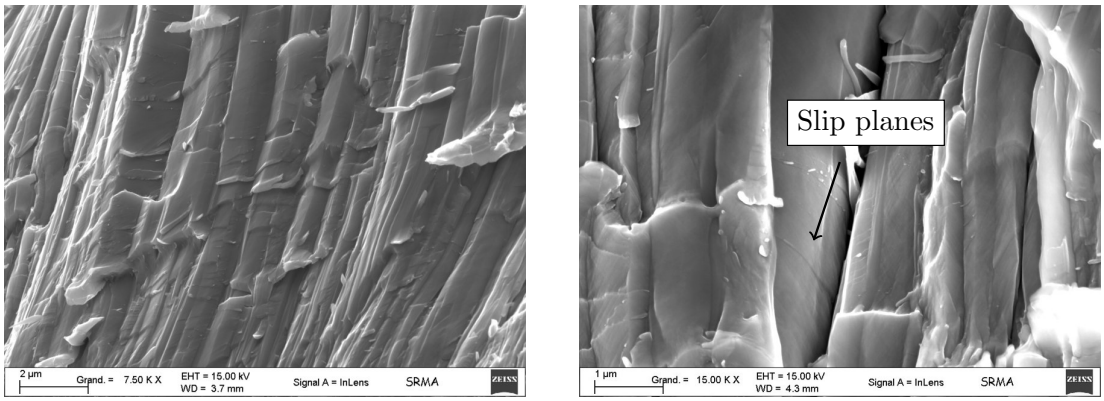

Figure 24: SEM images of fracture surfaces of the Cr coating in the necked region of a $M5_{Framatome}$ plate sample failed under *in situ* uniaxial tension in SEM.

of the tube [20].

The results show that the loading biaxiality has an effect on strains/stresses in the coating at the crack onset. The principal stresses in the coating at the crack onset can be estimated by supposing that the coating remains in the elastic regime before cracking and assuming plane stress condition. A Young's modulus of 290 GPa and a Poisson's coefficient of 0.22 [9, 24] are considered. The compressive residual stresses of a few hundred MPa in average in the coating are not taken into account so that the stress values reported include the initial residual stresses. The formula used are given in Appendix. The results are reported in Table 2. It is observed that the Cr coating starts to crack when its maximum principal stress exceeds a certain value of about 1100 MPa, except for the case of hoop tension ($\alpha = 0$) where the critical value is a little higher. This difference could be related to a difference in residual stresses in the two in-plane directions.

The evolution of crack density as function of applied strain is rather similar for the axial tensile test on tube and the tensile test on plate sample (Fig. 19b), despite a different geometry (sheet vs. tube) and a different substrate thickness (0.57 mm coated on one side for tube samples vs. 1.1 mm coated on two sides for the sheet sample). In addition, the loading direction is parallel to the rolling direction for the tube whereas it is perpendicular for the plate sample. Thus, the plastic anisotropy of the Zr alloy substrate seems to have negligible effect on the strained-induced crack densification in the coating. Higher crack onset strain and lower crack density at saturation are observed for axial tension than for hoop tension on tubes. In addition, in the case of equi-biaxial stress state on coated tube, cracks which propagate in the hoop direction are rather long and straight as these cracks, as shown by DIC, initiate first and are able to propagate freely without interaction with other cracks before being connected at larger applied strain by shorter

cracks. The plastic anisotropy of the substrate alone can not explain this difference. The fact that the Cr coating is more resistant to formation of axial cracks than of hoop cracks can be related to a geometrical effect (the curvature of the tube) or to non-equibiaxial residual stresses in the coating.

In the case of axial tension and biaxiality ratio of 2 on tubes, the long cracks which propagate over more than half of the tube circumference are probably the first cracks that propagate in the coating in such a way that their propagation is not influenced by other cracks. At larger applied strain, cracks probably tend to stop propagating when they approach another crack nearby, due to stress relaxation in the coating in the presence of pre-existing cracks. Likewise, the absence of narrower uncracked regions is expected to be the consequence of interactions between adjacent cracks.

The high level of strain of the Cr coating measured both directly by DIC and indirectly from the crack opening show that, after having cracked in a rather brittle manner, the coating deforms plastically after cracking saturation. The traces of dislocation slip planes observed in the coating's fracture surface also show that Cr grains are able to deform plastically to some extent at room temperature. The strain localization bands observed at the surface of the coating are probably imposed by plastic strain localisation in the Zr-based substrate [35]. This plastic strain of the substrate is also indicated by the relatively blunt tips of the cracks in the coating observed on sample cross-sections.

5. Conclusions

Biaxial tests (internal pressure + axial tension) with several biaxiality ratios and *in situ* tensile tests in SEM were performed at room temperature on ∼0.57 mm-thick tube and ∼1.2 mm-thick sheet samples made of $M5_{Framatome}$ (Zr-based) with a ∼15 ÂţmÂţm-thick coating deposited using a particular PVD-type process. The coating cracking was studied using high resolution DIC, AE measurement, optical microscopy and SEM observation. The Cr coating has minor effect on the macroscopic mechanical behavior of the coated material. Channeling cracks propagate in the coating at about 0.4% macroscopic strain under uniaxial loading. The crack onset strain depends on stress biaxiality. The Cr coating starts to crack approximately at the beginning of substrate plastic yielding. When the maximum principal stress component in the coating exceeds about 1075 ± 75 MPa, cracks initiate and propagate preferentially in the orthogonal direction, from which the compressive residual stresses in the coating of typically a few hundred MPa should be subtracted to estimate the intrinsic mean critical stress. The cracks propagate through the thickness of the coating but do not penetrate into the substrate. The crack density increases rapidly after the first cracks appear but reaches saturation after a few percent of applied strain. The Cr coating first cracks in a rather brittle manner and then exhibits plastic deformation. Good adherence between the coating and the substrate is demonstrated.

The first perspective to this work would be to go further in the interpretation of the results obtained, in particular to explain the saturation of coating cracking and to study the influences of residual stresses, plastic strain of the substrate and plasticity of the coating on cracking. This could be done through numerical simulation. Then, the methodology developed here could be applied to study the behavior of the coating when the cladding is loaded at higher temperatures, especially at the cladding in-service temperature (∼ 350ÂřC). In this range of temperature, the Cr coating exhibits more plasticity and thus higher ductility. Moreover, the effect of heat treatment and of irradiation, that should change the materials state, is worth being considered.

Acknowledgements

We thank EDF and Framatome for their contributions to this work. This work was funded by the CEA-Framatome-EDF French Nuclear Institute.

Data Availability

The raw/processed data required to reproduce these findings cannot be shared at this time due to technical or time limitations.

Appendix

The following formula are used to calculate the principal stresses in the coating at the crack onset (written in the cylindrical coordinate system), where E and ν are respectively the Young's modulus and the Poisson's coefficient of

the coating :

$$\underline{\underline{\varepsilon}} = \begin{pmatrix} \varepsilon_{rr} & 0 & 0 \\ 0 & \varepsilon_{\theta\theta} & 0 \\ 0 & 0 & \varepsilon_{zz} \end{pmatrix} = \begin{pmatrix} \frac{\nu}{\nu-1}(\varepsilon_{zz}+\varepsilon_{\theta\theta}) & 0 & 0 \\ 0 & \varepsilon_{\theta\theta} & 0 \\ 0 & 0 & \varepsilon_{zz} \end{pmatrix}$$

$$\underline{\underline{\sigma}} = \begin{pmatrix} \sigma_{rr} & 0 & 0 \\ 0 & \sigma_{\theta\theta} & 0 \\ 0 & 0 & \sigma_{zz} \end{pmatrix} = \frac{E}{1+\nu} \begin{pmatrix} 0 & 0 & 0 \\ 0 & \varepsilon_{\theta\theta} + \frac{\nu}{1-\nu}(\varepsilon_{zz}+\varepsilon_{\theta\theta}) & 0 \\ 0 & 0 & \varepsilon_{zz} + \frac{\nu}{1-\nu}(\varepsilon_{zz}+\varepsilon_{\theta\theta}) \end{pmatrix}$$

References

[1] S. J. Zinkle, K. A. Terrani, J. C. Gehin, L. J. Ott, L. L. Snead, Accident tolerant fuels for LWRs: A perspective, Journal of Nuclear Materials 448 (1) (2014) 374–379. doi:10.1016/j.jnucmat.2013.12.005.
URL http://www.sciencedirect.com/science/article/pii/S0022311513012919

[2] K. A. Terrani, Accident tolerant fuel cladding development: Promise, status, and challenges, Journal of Nuclear Materials 501 (2018) 13–30. doi:10.1016/j.jnucmat.2017.12.043.
URL http://www.sciencedirect.com/science/article/pii/S0022311517316227

[3] C. Tang, M. Stueber, H. J. Seifert, M. Steinbrueck, Protective coatings on zirconium-based alloys as accident-tolerant fuel (ATF) claddings, Corrosion Reviews 35 (3) (2017) 141–165. doi:10.1515/corrrev-2017-0010.
URL https://www.degruyter.com/document/doi/10.1515/corrrev-2017-0010/html

[4] J.-C. Brachet, I. Idarraga-Trujillo, M. L. Flem, M. Le Saux, V. Vandenberghe, S. Urvoy, E. Rouesne, T. Guilbert, C. Toffolon-Masclet, M. Tupin, C. Phalippou, F. Lomello, F. Schuster, A. Billard, G. Velisa, C. Ducros, F. Sanchette, Early studies on Cr-Coated Zircaloy-4 as enhanced accident tolerant nuclear fuel claddings for light water reactors, Journal of Nuclear Materials 517 (2019) 268–285. doi:10.1016/j.jnucmat.2019.02.018.
URL http://www.sciencedirect.com/science/article/pii/S0022311518316519

[5] J. Bischoff, C. Delafoy, C. Vauglin, P. Barberis, C. Roubeyrie, D. Perche, D. Duthoo, F. Schuster, J.-C. Brachet, E. W. Schweitzer, K. Nimishakavi, AREVA NP's enhanced accident-tolerant fuel developments: Focus on Cr-coated M5 cladding, Nuclear Engineering and Technology 50 (2) (2018) 223–228. doi:10.1016/j.net.2017.12.004.
URL http://www.sciencedirect.com/science/article/pii/S1738573317307945

[6] J. C. Brachet, M. Le Saux, J. Bischoff, H. Palancher, R. Chosson, E. Pouillier, T. Guilbert, S. Urvoy, G. Nony, T. Vandenberghe, A. Lequien, C. Miton, P. Bossis, Evaluation of Equivalent Cladding Reacted parameters of Cr-coated claddings oxidized in steam at 1200ÂřC in relation with oxygen diffusion/partitioning and post-quench ductility, Journal of Nuclear Materials 533 (2020) 152106. doi:10.1016/j.jnucmat.2020.152106.
URL http://www.sciencedirect.com/science/article/pii/S0022311519314667

[7] J. C. Brachet, E. Rouesne, J. Ribis, T. Guilbert, S. Urvoy, G. Nony, C. Toffolon-Masclet, M. Le Saux, N. Chaabane, H. Palancher, A. David, J. Bischoff, J. Augereau, E. Pouillier, High temperature steam oxidation of chromium-coated zirconium-based alloys: Kinetics and process, Corrosion Science 167 (2020) 108537. doi:10.1016/j.corsci.2020.108537.
URL http://www.sciencedirect.com/science/article/pii/S0010938X19322565

[8] T. Wei, R. Zhang, H. Yang, H. Liu, S. Qiu, Y. Wang, P. Du, K. He, X. Hu, C. Dong, Microstructure, corrosion resistance and oxidation behavior of Cr-coatings on Zircaloy-4 prepared by vacuum arc plasma deposition, Corrosion Science 158 (2019) 108077. doi:10.1016/j.corsci.2019.06.029.
URL https://www.sciencedirect.com/science/article/pii/S0010938X18320407

[9] T. Tietz, J. W. Wilson, Behaviour and properties of refractory metals, Stanford University Press, 1965.

[10] J. C. Thornley, A. S. Wronski, The grain-size-dependences of the failure mode and ductility transition temperatures of melted chromium and tungsten, Metal Science Journal 6 (1972) 113–118.

[11] W. H. Smith, A. U. Seybolt, Ductile Chromium, Journal of The Electrochemical Society 103 (6) (1956) 347–352. doi:10.1149/1.2430326.
URL https://iopscience.iop.org/article/10.1149/1.2430326

[12] C. W. Weaver, StrainâĂŞAge Hardening and Brittleness in Chromium, Nature 180 (4590) (1957) 806–808. doi:10.1038/180806b0.
URL https://www.nature.com/articles/180806b0

[13] H. L. Wain, F. Henderson, S. T. M. Johnstone, A Study of the Room-Temperature Ductility of Chromium, Journal of the Institute of Metals 83 (1954) 133–142.

[14] C. L. Briant, K. S. Kumar, N. Rosenberg, H. Tomioka, The mechanical properties of high purity chromium, International Journal of Refractory Metals and Hard Materials 18 (1) (2000) 9–11. doi:10.1016/S0263-4368(99)00031-1.
URL http://www.sciencedirect.com/science/article/pii/S0263436899000311

[15] R. Wadsack, R. Pippan, B. Schedler, The effect of pre-deformation on the ductility of chromium, Journal of Nuclear Materials 307-311 (2002) 701–704. doi:10.1016/S0022-3115(02)00945-5.
URL http://www.sciencedirect.com/science/article/pii/S0022311502009455

[16] B. A. Wilcox, N. D. Veigel, A. H. Clauer, Ductile-brittle transition of thoriated chromium, Metallurgical and Materials Transactions B 3 (1)

(1972) 273–283. doi:10.1007/BF02680606.
URL https://link.springer.com/article/10.1007%2FBF02680606

[17] M. F. Doerner, W. D. Nix, Stresses and deformation processes in thin films on substrates, Critical Reviews in Solid State and Materials Sciences 14 (3) (1988) 225–268. doi:10.1080/10408438808243734.
URL https://www.tandfonline.com/doi/abs/10.1080/10408438808243734

[18] J. W. Hutchinson, Stresses and failure modes in thin films and multilayers, 1996.
URL https://www.seas.harvard.edu/hutchinson/papers/462-5.pdf

[19] J. Jiang, H. Zhai, P. Gong, W. Zhang, X. He, X. Ma, B. Wang, In-situ study on the tensile behavior of Cr-coated zircaloy for accident tolerant fuel claddings, Surface and Coatings Technology 394 (2020) 125747. doi:10.1016/j.surfcoat.2020.125747.
URL http://www.sciencedirect.com/science/article/pii/S0257897220304163

[20] D. C. Roache, A. Jarama, C. H. Bumgardner, F. M. Heim, J. Walters, J. Romero, B. Maier, X. Li, Unveiling damage mechanisms of chromium-coated zirconium-based fuel claddings by coupling digital image correlation and acoustic emission, Materials Science and Engineering: A 774 (2020) 138850. doi:10.1016/j.msea.2019.138850.
URL http://www.sciencedirect.com/science/article/pii/S0921509319316326

[21] J. Jiang, D. Zhan, J. Lv, X. Ma, X. He, D. Wang, Y. Hu, H. Zhai, J. Tu, W. Zhang, B. Wang, Comparative study on the tensile cracking behavior of CrN and Cr coatings for accident-tolerant fuel claddings, Surface and Coatings Technology 409 (2021) 126812. doi:10.1016/j.surfcoat.2020.126812.
URL https://www.sciencedirect.com/science/article/pii/S0257897220314821

[22] S. Yagnik, A. Garde, Chapter 7 - Zirconium Alloys for LWR Fuel Cladding and Core Internals, Elsevier, Boston, 2019, pp. 247–291. doi:10.1016/B978-0-12-397046-6.00007-1.

[23] A. Hellouin de Menibus, J. Sercombe, Q. Auzoux, C. Poussard, Thermomechanical loading applied on the cladding tube during the pellet cladding mechanical interaction phase of a rapid reactivity initiated accident, Journal of Nuclear Materials 453 (1) (2014) 210–213. doi:10.1016/j.jnucmat.2014.06.046.
URL http://www.sciencedirect.com/science/article/pii/B9780123970466000071

[24] U. Holzwarth, H. Stamm, Mechanical and thermomechanical properties of commercially pure chromium and chromium alloys, Journal of Nuclear Materials 300 (2) (2002) 161–177. doi:10.1016/S0022-3115(01)00745-0.
URL http://www.sciencedirect.com/science/article/pii/S0022311501007450

[25] J. C. Brachet, A. Billard, F. Shuster, M. Le Flem, I. Idarraga-Trujillo, M. Le Saux, F. Lomello, Nuclear fuel claddings, production method thereof and uses of same against oxidation/hydriding, Patent Application Publication No. US 2017/0287578 A1, 2017.

[26] B. Maier, H. Yeom, G. Johnson, T. Dabney, J. Walters, J. Romero, H. Shah, P. Xu, K. Sridharan, Development of Cold Spray Coatings for Accident-Tolerant Fuel Cladding in Light Water Reactors, JOM 70 (2) (2018) 198–202. doi:10.1007/s11837-017-2643-9.
URL https://link.springer.com/article/10.1007%2Fs11837-017-2643-9

[27] J. Ribis, A. Wu, J. Brachet, F. Barcelo, B. Arnal, Atomic-scale Interface structure of a Cr-coated Zircaloy-4 material, Journal of Materials Science 53. doi:10.1007/s10853-018-2333-1.
URL https://hal-cea.archives-ouvertes.fr/cea-02415674

[28] T. C. Reiley, W. D. Nix, The structure and mechanical properties of physically vapor deposited chromium, Metallurgical Transactions A 7 (11) (1976) 1695–1701. doi:10.1007/BF02817887.
URL https://link.springer.com/article/10.1007%2FBF02817887

[29] C. Gautier, J. Machet, Effects of deposition parameters on the texture of chromium films deposited by vacuum arc evaporation, Thin Solid Films 289 (1) (1996) 34–38. doi:10.1016/S0040-6090(96)08891-8.

[30] J. Pina, A. Dias, M. FranÃğois, J. L. Lebrun, Residual stresses and crystallographic texture in hard-chromium electroplated coatings, Surface and Coatings Technology 96 (2) (1997) 148–162. doi:10.1016/S0257-8972(97)00075-3.
URL http://www.sciencedirect.com/science/article/pii/S0257897297000753

[31] F. Onimus, M. Bono, J. Garnier, A. Soniak-Defresne, R. Limon, D. Gilbon, F. Bourlier, A. Ambard, Strain-Path Change Tests and Physically Based Polycrystalline Modeling of the Behavior of Recrystallized Zirconium Alloys, Zirconium in the Nuclear Industry: 18th International Symposium ASTM STP1597 (2018) 180–213. doi:10.1520/STP159720160092.
URL http://www.astm.org/DIGITAL_LIBRARY/STP/PAGES/STP159720160092.htm

[32] M. Bornert, F. BrÃľmand, P. Doumalin, J.-C. DuprÃľ, M. Fazzini, M. GrÃľdiac, F. Hild, S. Mistou, J. Molimard, J.-J. Orteu, L. Robert, Y. Surrel, P. Vacher, B. Wattrisse, Assessment of Digital Image Correlation Measurement Errors: Methodology and Results, Experimental Mechanics 49 (3) (2008) 353–370. doi:10.1007/s11340-008-9204-7.
URL https://link.springer.com/article/10.1007/s11340-008-9204-7

[33] M. Bornert, P. Doumalin, J.-C. DuprÃľ, C. PoilÃćne, L. Robert, E. Toussaint, B. Wattrisse, Assessment of Digital Image Correlation Measurement Accuracy in the Ultimate Error Regime: Improved Models of Systematic and Random Errors, Experimental Mechanics 58 (1) (2018) p.33–48. doi:10.1007/s11340-017-0328-5.
URL https://hal.archives-ouvertes.fr/hal-01577239

[34] V. A. Belous, S. V. Gozhenko, Y. A. Krainyuk, A. S. Kuprin, V. D. Ovcharenko, V. I. Savchenko, S. V. Shramchenko, Effect of chromium coatings on the mechanical properties of Zr1Nb fuel claddings in longitudinal and transverse directions, Problems of atomic science and technology 123 (5) (2019) 142–146.
URL https://www.researchgate.net/publication/336371069

[35] K. Elbachiri, P. Doumalin, J. CrÃľpin, M. Bornert, P. Barberis, V. Rebeyrolle, T. Bretheau, Characterization of Local Strain Distribution in Zircaloy-4 and M5 Alloys, Journal of ASTM International 5 (9) (2008) 1–11. doi:10.1520/JAI101125.
URL http://www.astm.org/DIGITAL_LIBRARY/JOURNALS/JAI/PAGES/JAI101125.htm

Declaration of Competing Interest

The authors declare that they have no known competing financial interests or personal relationships that could have appeared to influence the work reported in this paper.

Credit Author Statment

Duc Vinh Nguyen: Conceptualization, Investigation, Validation, Writing - original draft, Visualization.
Matthieu Le Saux: Conceptualization, Validation, Writing - review & editing, Supervision.
Lionel Gélébart: Conceptualization, Validation, Writing - review & editing, Supervision.
Jean-Christophe Brachet: Conceptualization, Validation, Writing - review & editing, Supervision.
Jean-Philippe Bonthonneau: Investigation.
Arnaud Courcelle: Investigation.
Raphaelle Guillou: Investigation.
Elodie Rouesne: Investigation.
Stephane Urvoy: Investigation.